

# Theory of epithelial sheet morphology in three dimensions

Edouard Hannezo<sup>a,1</sup>, Jacques Prost<sup>a,b</sup>, and Jean-François Joanny<sup>a</sup>

<sup>a</sup>Physicochimie Curie (Institut Curie/Centre National de la Recherche Scientifique–Unité Mixte de Recherche 168/UPMC), Institut Curie, Centre de Recherche, 75248 Paris Cedex 05, France; and <sup>b</sup>Ecole Supérieure de Physique et de Chimie Industrielles, 75231 Paris Cedex 05, France

Edited by Robert H. Austin, Princeton University, Princeton, NJ, and approved November 19, 2013 (received for review June 26, 2013)

**Morphogenesis during embryo development requires the coordination of mechanical forces to generate the macroscopic shapes of organs.** We propose a minimal theoretical model, based on cell adhesion and actomyosin contractility, which describes the various shapes of epithelial cells and the bending and buckling of epithelial sheets, as well as the relative stability of cellular tubes and spheres. We show that, to understand these processes, a full 3D description of the cells is needed, but that simple scaling laws can still be derived. The morphologies observed *in vivo* can be understood as stable points of mechanical equations and the transitions between them are either continuous or discontinuous. We then focus on epithelial sheet bending, a ubiquitous morphogenetic process. We calculate the curvature of an epithelium as a function of actin belt tension as well as of cell-cell and cell-substrate tension. The model allows for a comparison of the relative stabilities of spherical or cylindrical cellular structures (acini or tubes). Finally, we propose a unique type of buckling instability of epithelia, driven by a flattening of individual cell shapes, and discuss experimental tests to verify our predictions.

mathematical modeling | active foams | biophysics

**U**nderstanding the development and stability of well-defined morphologies in mature epithelial tissues is an important challenge. During embryogenesis, epithelial sheets undergo extensive and precise morphological changes, which generate the 3D structure of organs (1–3). Metaplasia, which is the conversion from one cell morphology to another one, is associated with several cancers (4). It is widely acknowledged that adhesion and cytoskeleton contractile forces, mediated by the Rho family GTPases, play an important role in the determination of cell shape (3, 5), development (2, 6), and cancer initiation (7). Although much is known about the underlying genetic regulation of these events (2, 7, 8) and although new experimental tools have allowed their quantitative measurements (9, 10), a global understanding of the physical mechanisms shaping a tissue remains elusive (3).

Theoretical efforts on epithelial morphology have largely focused on 2D models of the top (apical) surface of cell sheets [with some exceptions considering 2D models of cell heights with tensile forces (11, 12)]. They have been used, for instance, to deduce the geometric arrangement of cell-cell apical junctions (5, 13–15) or the out-of-plane buckling of apical surfaces (16). Nevertheless, morphogenesis and cellular shape changes are intrinsically 3D processes, for which both lateral and basal tensions also play a role (2, 17, 18), so 2D approaches cannot tackle many important morphogenetic events.

In this article, we present a minimal model that can explain, with few and measurable parameters associated with adhesion and contractile forces (Fig. 1), several aspects of epithelial cell shape and tissue morphology. We first discuss epithelial cell aspect ratio in three dimensions on a flat substrate, considering three types of cells: tall and thin, (columnar), flat and spread out (squamous), or an intermediate cuboidal shape (2). We then calculate the spontaneous curvature adopted by a cell sheet as a function of cell-substrate and cell-cell tensions and contractile forces from the apical actin belt. This sheds light on the stability of cellular

structures, such as spheres or tubes, and on the epithelial sheet bending involved in a wide variety of developmental processes (3, 9, 10), including gastrulation and neural tube, ventral furrow, and lens placode formation. Finally, we show how varying cell adhesion or actomyosin constriction above a certain threshold in a confined environment can cause an epithelial sheet to buckle, as observed during the development of the *Drosophila* wing disk (19). For each of these phenomena, we give scaling laws that could serve as simple guides for future experiments.

## Morphologies of Planar Epithelial Cells

We model epithelial cells as hexagonal prisms of base length  $r$  and height  $h$ . We consider only cohesive sheets and, at first, we do not implement any constraint on the total area of the sheet. Considering all cells as identical, we write the force balance equation on a single cell, which we consider planar in this section. We deliberately forget about the detailed topography of the cell-cell junctions, which was described in two dimensions in ref. 14 to focus on generic scaling arguments. Although the tissue is an out-of-equilibrium system, it is convenient to write the mechanical equilibrium at steady state as the minimization of a work function, or effective energy  $\mathcal{F}$ , where the nonequilibrium aspect is hidden in the tensions (Fig. S1). We define a cell as columnar when  $\frac{h}{r} \gg 1$ , cuboidal when  $\frac{h}{r} \approx 1$  and squamous when  $\frac{h}{r} \ll 1$ .

Epithelial cells display an apico-basal polarity (1): The adhesion with the substrate defines the basal surface, whereas a contractile actomyosin belt often forms on the upper, apical surface. We thus consider the following contributions to the effective energy: a cell-substrate energy, proportional to the basal area,  $\gamma_b A_{\text{basal}}$ ; a cell-cell lateral energy, proportional to the lateral area,  $\gamma_l A_{\text{lateral}}$ ; and an energy associated to the tension of the apical actomyosin belt  $\Lambda_a$ , proportional to the apical perimeter,  $\Lambda_a P_{\text{ap}}$ .

## Significance

**Epithelia are the tissue layers that line organs throughout the body. Their complex movements and extensive reorganization have been widely studied as a model system of embryo development. Epithelial cells have been theoretically described using physical models close to those used for soap bubbles and foams. Nevertheless, although morphogenesis is intrinsically three-dimensional, previous works have mostly considered a two-dimensional planar geometry. In this paper, we provide a theoretical three-dimensional description of epithelial sheets, which describes within a single framework many developmental transitions, such as the formation of cavities or cellular tubes of a given size. We provide simple scaling laws that could be verified experimentally, for each of these transitions.**

Author contributions: E.H., J.P., and J.-F.J. designed research, performed research, and wrote the paper.

The authors declare no conflict of interest.

This article is a PNAS Direct Submission.

<sup>1</sup>To whom correspondence should be addressed. E-mail: edouard.hannezo@curie.fr.

This article contains supporting information online at [www.pnas.org/lookup/suppl/doi:10.1073/pnas.1312076111/-DCSupplemental](http://www.pnas.org/lookup/suppl/doi:10.1073/pnas.1312076111/-DCSupplemental).

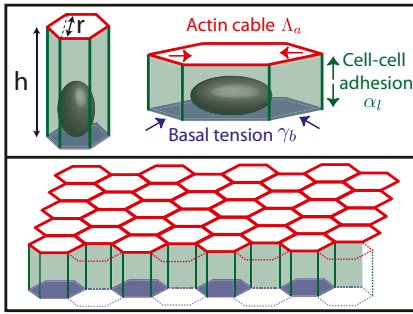


Fig. 1. Sketch of our theoretical model.

The lateral tension  $\gamma_l$  is the sum of several contributions of opposite signs (20): a positive contribution from contractile forces of the actomyosin lateral cortex, which tends to minimize the lateral surface, and a negative contribution from the adhesion with the neighboring cells, which tends to maximize the lateral surface. The tensions could also have contributions from external stresses. Thus, the tensions  $\gamma_l$  and  $\gamma_b$  are either positive or negative.

For practical reasons, we define and use  $\alpha_l = -\gamma_l$ , the effective lateral adhesion, in the rest of the article. Moreover, although tension often dominates in the actin cable (3), we study the case of either positive or negative  $\Lambda_a$  for completeness. We assume that the cells have a preferred volume  $V_0$  and we expand the effective energy around  $V_0$ . The first contribution is  $B(V - V_0)^2$ , where  $V$  is the cell volume and  $B$  a compression modulus. Therefore, our effective energy reads

$$\mathcal{F} = \gamma_b A_{\text{basal}} - \alpha_l A_{\text{lat}} + \Lambda_a P_{\text{ap}} + \frac{B}{V_0} (V - V_0)^2. \quad [1]$$

If the compression modulus is large ( $B \rightarrow \infty$ ),  $V$  is constant and equal to  $V_0$ , as observed during several morphological changes (8, 10) (the case of finite  $B$  is treated in *SI Text* and does not change qualitatively the results). This yields a geometrical relationship between  $r$  and  $h$ :  $h = \frac{2V_0}{\sqrt{3}r^2}$ .

In the case  $\alpha_l > 0$ ,  $\gamma_b < 0$ , the two configurations that minimize the effective energy from Eq. 1 are then either infinitely thin and spread cells ( $r \rightarrow \infty, h \rightarrow 0$ ) or infinitely tall cells ( $r \rightarrow 0, h \rightarrow \infty$ ). Therefore, an additional stabilizing term is necessary, as observed in ref. 20. Because it has been shown that the cytoskeleton is an important determinant of cell shape (21), we stress that a cell is a dense solution of cytoplasmic components, which cannot be indefinitely squeezed (20). Notably, intermediate filaments are known to function as a stress-bearing structure (22). We show in the next section through simple orders of magnitude that it could be a sufficient stabilizing mechanism. Moreover, the cell nucleus is a rigid object and is deformed when cells are confined (23). The confinement of a solution of nonadsorbing Gaussian polymers to a thickness  $h$  requires an energy  $\frac{A}{h^2}$  (24), where  $A$  is a coefficient dependent on the properties of the polymer. When cells become very tall ( $r \rightarrow 0$ ), the same confinement energy should be included:  $2\frac{A}{r^2}$ . We discuss other hypotheses in the next section and in *SI Text*.

To eliminate the prefactors coming from the hexagonal geometry, we choose  $\frac{4^{1/6}}{3} V_0^{1/3}$  as the unit length and  $\frac{3^{1/3}}{4} \frac{A}{V_0^{2/3}}$  as the unit energy (details in *SI Text*). We obtain a simple equation, with only three rescaled parameters, which we rename  $\frac{2^{1/3}}{3^{1/6}} \frac{\gamma_b V_0^{4/3}}{A} \rightarrow \gamma_b$ ,  $\frac{3^{1/6} 4^{5/6} \alpha_l}{A V_0^{2/3}} \rightarrow \alpha_l$ , and  $\frac{2^{5/3} 3^{1/3} \Lambda_a V_0}{A} \rightarrow \Lambda_a$ :

$$\mathcal{F} = \gamma_b r^2 - \frac{\alpha_l}{r} + \Lambda_a r + r^4 + \frac{2}{r^2}. \quad [2]$$

The minimum of this energy function ( $\frac{d\mathcal{F}}{dr} = 0$ ) defines the cell base length at mechanical equilibrium.

**Assumption of the Model.** Our main assumption is the form of the confinement energy of the cytoplasmic components written as  $\mathcal{E} = \frac{1}{h^n} + \frac{2}{r^m}$ , which is the confinement energy of Gaussian polymers. Other assumptions on the nature of the cytoplasmic components, or on a precise rheology of the nucleus, would yield different power laws of the form  $\mathcal{E}_{\text{repuls}} = \frac{1}{h^n} + \frac{2}{r^m}$ . For instance, it has been argued that semiflexible polymers correspond, in the high-confinement limit, to  $n = 7/2$  (25). Nevertheless, it should be noted that several scaling laws we derive (Eqs. 5 and 6), as well as the main features of the phase diagrams, are model independent and hold for any value of the exponent  $n$ . On the other hand, some scaling laws are model dependent. We derive them for any  $n$  and draw the phase diagrams for various values of  $n$  in *SI Text* and Fig. S2. An alternative stabilizing mechanism could be an active regulation of the tensions to achieve some target basal and lateral areas  $A_b^0$  and  $A_{\text{lat}}^0$ . Then, expanding the tensions around these target areas to first order [ $\gamma_b = \gamma_b^0 + \delta_1(r^2 - A_b^0)$  and  $\alpha_l = \alpha_l^0 - \delta_2(\frac{V_0}{r} - A_{\text{lat}}^0)$ ] yields the same stabilizing terms as our model, as long as the coefficients  $\delta_1, \delta_2$  are positive. In *SI Text* and Fig. S3, we show that the results of the main text are not qualitatively modified by assuming an active regulation of the tensions.

**Stable Epithelial Cell Aspect Ratios.** In our model, cell–cell lateral adhesion ( $\alpha_l > 0$ ) and apical belt tension favor tall columnar cells, whereas cell–cell contractile forces ( $\alpha_l < 0$ ) and cell–substrate adhesion ( $\gamma_b < 0$ ) favor squamous cells, in agreement with the experimental observations that squamous cells down-regulate E-cadherin and Fas2/3 (cell–cell adhesion) (17, 18), whereas columnar cells up-regulate E-cadherin expression and down-regulate cell–matrix adhesion (2, 18).

More precisely, from Eq. 2, we give analytical limits for cell aspect ratios. If cell–substrate adhesion is dominant ( $\gamma_b < 0$  and  $|\gamma_b| \gg 1$ ), cells are squamous and spread to a base length  $r \approx \sqrt{-\frac{\gamma_b}{2}} \gg 1$ . If cell–cell adhesion is dominant ( $\alpha_l > 0$  and  $|\alpha_l| \gg 1$ ), cells are columnar and the stable base length is  $r \approx \frac{1}{\alpha_l} \ll 1$ . If cell–cell contractile forces are dominant ( $\alpha_l < 0$  and  $|\alpha_l| \gg 1$ ), cells are squamous and the stable base length is  $r \approx (\frac{-\alpha_l}{4})^{1/5} \gg 1$ . Finally, if apical contractile forces are dominant ( $\Lambda_a \gg 1$ ), cells are columnar and the stable base length is  $r \approx \frac{2}{\sqrt{\Lambda_a}} \ll 1$ .

We now estimate the parameters of the model. The main unknown is the confinement energy of the cytoplasmic components  $A$ . In vitro experiments on the confinement of actin chains (25), as well as rheological measurements on *Xenopus* egg cytoplasmic extracts (26), suggest an order of magnitude of  $A \approx 10^{-24} - 10^{-23} \text{ J} \cdot \text{m}^2$  (*SI Text*). Although the complete cytoskeleton in a living cell is much more complex and can partially reorganize when the cell morphology changes, using a lower bound value, with typical values of the cell surface energies  $\gamma_b$  and  $\alpha_l$  of  $10^{-4} \text{ N/m}$  (27) would predict a base length of squamous cells  $r = \sqrt{\frac{-\gamma_b}{24}} V_0$  of order  $\approx 25 \mu\text{m}$ , with a cellular height  $h \approx 2 \mu\text{m}$ . These estimates are close to the observed values for a cell of volume  $V_0 \approx 10^{-15} \text{ m}^3$  (28) and suggest that this confinement contribution could be large enough to stabilize cell spreading to a realistic height. Moreover, for an apical belt of transverse radius  $l_a$ , the typical line tension is  $\Lambda_a = \Pi l_a^2$ , where  $\Pi$  is the characteristic contractile stress of actomyosin cables that can be estimated from laser-cutting experiments (29). Reported

values are  $l_a = 1 \mu\text{m}$  and  $\Pi = 10^3 - 10^4 \text{ Pa}$ , so  $\Lambda_a \approx 1 - 10 \text{ nN}$  (30). Then, in our renormalized units, we deduce  $|\gamma_b| \approx 10$ ,  $|\alpha_l| \approx 10$ , and  $\Lambda_a \approx 1 - 10$  and calculate the following phase diagrams using parameters within this regime.

**Shape Transitions in Epithelia.** When the parameters are varied continuously, the transition from columnar to squamous cells can be either smooth or discontinuous, typical of a bistable system. Fig. 2 A and B shows the two possible profiles of the effective energy  $\mathcal{F}$ , for increasing  $\Lambda_a$ : either one minimum  $r$ , continuously decreasing with increasing  $\alpha_l$ , or two distinct minima corresponding to squamous and columnar morphologies.

The observed morphologies of epithelial cells are therefore found as the stable points of a force balance equation and there are nontrivial transitions between aspect ratios. The appearance of a new stable point occurs if  $\frac{d\mathcal{F}}{dr} = \frac{d^2\mathcal{F}}{dr^2} = 0$ , a condition that defines the so-called spinodal lines, separating regions with one stable aspect ratio from regions with two stable aspect ratios. We perform a numerical integration of these equations to obtain the phase diagram of epithelial aspect ratio, plotted in a plane ( $\alpha_l - \Lambda_a$ ) for  $\gamma_b = -15$  (Fig. 2B), and derive scaling laws for various values of  $\gamma_b$  near the critical point (Fig. S4).

This model agrees qualitatively with a wide range of experimental data. Notably, many epithelial shape changes feature an apical constriction, regulated by RhoA (9). We predict that the tension in the apical belt  $\Lambda_a$ , as well as the cell-cell lateral adhesion, is a crucial parameter to establish a mature columnar epithelium. Indeed, either down-regulating the apical myosin IIb through blebbistatin (31) or lowering the lateral cell-cell interaction through Tmod3 (8) decreases cell height by about 30%.

We also predict that, depending on the parameters, one should observe either a progressive cuboidal to columnar transition, as in *Drosophila* wing morphogenesis (19) (mediated by the Dpp-Rho1-myosin IIb pathway, which again up-regulates the apical tension), or a sharp squamous to columnar transition, as in Barrett's metaplasia before stomach cancer (4). A stronger, quantitative test would be to quantify the aspect ratio of epithelial cells while varying smoothly myosin activity, for instance using a control parameter that could be blebbistatin concentration.

Finally, rewriting the effective energy from Eq. 2 as a function of cellular perimeter  $\mathcal{P}$  and apical surface  $\mathcal{A}_{ap}$ , we can compare our 3D effective energy to previous 2D theories  $\mathcal{F} = \Lambda_a \mathcal{P} + (\mathcal{A}_{ap} - \mathcal{A}_0)^2 - \alpha_l \frac{\mathcal{P}}{\mathcal{A}_{ap}} + \frac{1}{\mathcal{A}_{ap}}$ . The first two terms are the same as in ref. 14, where  $\mathcal{A}_0 = -\gamma_b/2$ . In the limit of low lateral adhesion  $|\alpha_l| \ll \Lambda_a \mathcal{A}_{ap}$ , the following two terms are negligible and

considering only the 2D apical surface is a valid approximation. Nevertheless, lateral adhesion must always be taken into account for very columnar and thin cells ( $\mathcal{A}_{ap} \rightarrow 0$ ).

### Epithelial Sheet Bending

We now examine 3D deformations of a cell sheet, without introducing any new parameters. The forces from basal tension and apical belt tension are not in the same location. If the substrate can deform, cells therefore adopt a “lampshade” shape (Fig. 3A), which leads to a spontaneous curvature of the epithelial sheet. This curvature can be either positive or negative, depending on the relative values of apical belt tension and the basal tension (Fig. 4 and Fig. S5). We discuss in *SI Text* (Fig. S5) a more precise analytical criterion for the curvature sign.

If all cells have the same morphology, the tissue bends and its global shape can be deduced from the individual cell properties. It is useful to define, in analogy to the theory of surfactants (32), the spontaneous curvature of asymmetric cells, i.e., the curvature of the cellular sphere that they would spontaneously form,

$$\mathcal{C} = \frac{r_1 - r_2}{r_2 h}, \quad [3]$$

where  $h$  is the height of a cell as before, and  $r_1$  and  $r_2$  are, respectively, the characteristic length of the cell apical and basal surface.

Considering as before a constant volume  $V_0$ , the effective energy of a cell (*SI Text*) is

$$\begin{aligned} \mathcal{F}_s = & -\frac{3\alpha_l}{2} \frac{r_1 + r_2}{r_1^2 + r_2^2 + r_1 r_2} + \frac{A}{9} (r_1^2 + r_2^2 + r_1 r_2)^2 + \frac{2A}{r_1^2} \\ & + \gamma_b r_1^2 + \Lambda_a r_2. \end{aligned} \quad [4]$$

We include a bending force from the substrate in *SI Text* (Fig. S6). The cell shape asymmetry is driven by the contributions of  $\gamma_b$  and  $\Lambda_a$  to the effective energy.

If  $\gamma_b = \Lambda_a = 0$ , the cell sheet is planar and the analysis of the previous section holds. When  $\gamma_b$  or  $\Lambda_a$  increases,  $r_1$  and  $r_2$  become increasingly different. There are two limiting cases, as  $\gamma_b$  or  $\Lambda_a$  is increased: a smooth increase of the curvature or an abrupt transition from a flat to a curved sheet (Fig. 3B). We first set  $\gamma_b = 0$  and examine the impact of the actin belt tension  $\Lambda_a$ , whose importance is most often emphasized (1), and consider  $\gamma_b$  in *SI Text* (Figs. S5 and S7).

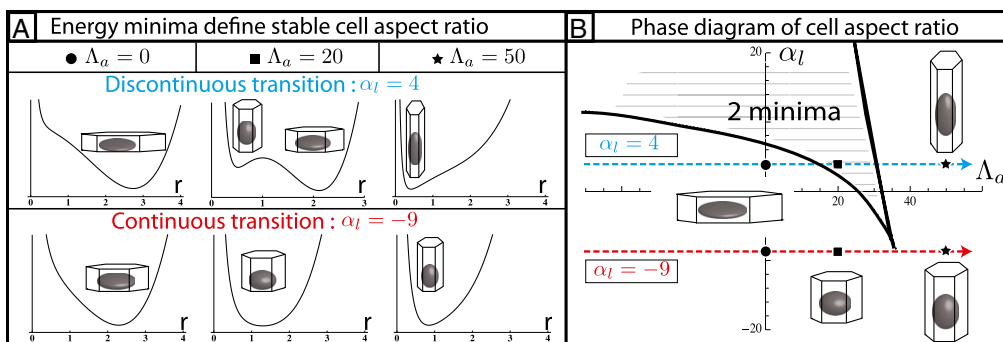


**Fig. 2.** Epithelial cell aspect ratio as a bistable phenomenon. (A) Plots of the effective energy of a cell as a function of the cell base length  $r$ , when apical belt tension  $\Lambda_a$  is increased (Left to Right). If contractile forces dominate  $\alpha_l$ , only one minimum of the energy, cells go continuously from squamous to cuboidal to columnar aspect ratios. If lateral adhesion is large enough ( $\alpha_l$  negative), two minima, cells “jump” from squamous to columnar aspect ratios. (B) Phase diagram as a function of  $\Lambda_a$  and  $\alpha_l$  for  $\gamma_b = -15$ , showing regions of continuous and discontinuous transitions.

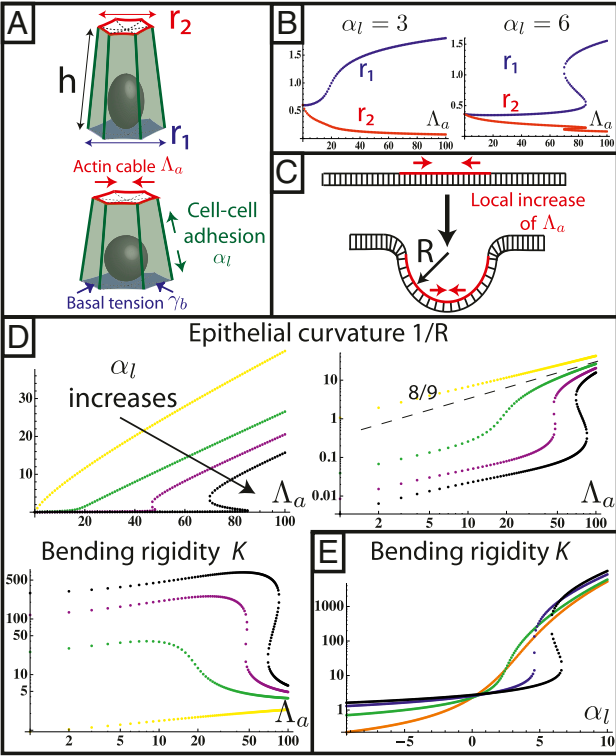


**Fig. 3.** Spontaneous curvature of an apically constricted tissue. (A) Sketch of our model. The cell is modeled as part of a sheet of constant height  $h$  between apical and basal sides. (B) Numerical integration of  $r_1$  and  $r_2$  as a function of apical belt tension  $\Lambda_a$ . (C) Sketch of a biological application: lens placode formation. The apical belt tension is increased locally, causing the tissue to invaginate with radius of curvature  $R$ . (D) Curvature and bending rigidity of the cell sheet as a function of apical belt tension  $\Lambda_a$  for various values of  $\alpha_l = -2$  (yellow),  $\alpha_l = 3$  (green),  $\alpha_l = 4.5$  (purple), and  $\alpha_l = 5.5$  (black). Note the change in convexity as  $\alpha_l$  changes sign. (E) Bending rigidity as a function of cell-cell adhesion, for various values of  $\Lambda_a = 0$  (orange),  $\Lambda_a = 10$  (green),  $\Lambda_a = 50$  (blue), and  $\Lambda_a = 100$  (black).

**Curvature Induced by an Apical Belt Tension.** We determine numerically the mechanical equilibrium defined as  $\frac{d\mathcal{F}}{dr_1} = \frac{d\mathcal{F}}{dr_2} = 0$ . We assume that the lateral adhesion dominates ( $\alpha_l > 0$ ); therefore, the epithelium is columnar. When the lateral adhesion increases, the curvature  $\mathcal{C}$  of the epithelium decreases (Fig. 3D), because lateral adhesion favors symmetrical shapes. We derive scaling laws for two limiting cases of small and high curvatures:  $\Lambda_a \ll \alpha_l$  and  $\Lambda_a \gg \alpha_l$ .

If  $\Lambda_a \ll \alpha_l$ , we rewrite  $r_2 = r_1 - \epsilon$  and expand the effective energy in powers of  $\frac{\epsilon}{r_1} \ll 1$ . We find

$$\mathcal{C} \propto \frac{\Lambda_a}{\alpha_l^5}. \quad [5]$$

In the opposite limit,  $\Lambda_a \gg \alpha_l$ , we obtain  $r_1 \propto \Lambda_a^{1/9}$ ,  $r_2 \propto \Lambda_a^{-5/9}$ . The curvature is slightly sublinear:  $\mathcal{C} \propto \Lambda_a^{8/9}$ . These theoretical predictions agree qualitatively with the experiments of ref. 9, showing that the curvature of an epithelium increases (resp. decreases) with a higher (resp. lower) recruitment of myosin IIb and P-MLRC at the apex of the cell.

They could be tested quantitatively by measuring the curvature of an epithelial monolayer and comparing it to the stress in the apical belt from laser-cutting experiments. Alternatively, mimicking an apical constriction on a collagen scaffold on known mechanical properties (33) could allow for a noninvasive, quantitative measurement of bending forces. Even simpler, for any exponent  $n$  in the confinement energy, the scaling law

$$r_1 \propto r_2^{-1/5} \quad [6]$$

holds in the limit of high constriction, which could be tested without any need to measure tensions.

It is useful to define an effective bending rigidity  $K_{\text{eff}} = \frac{\Lambda_a}{\mathcal{C}}$  of the epithelial sheet, which quantifies the resistance of a cell layer to the apical constriction. A strength of our model is that we calculate this quantity from a realistic microscopic model and do not assume it a priori. For  $\Lambda_a \ll \alpha_l$ , the bending rigidity is constant (Fig. 3D) and depends very strongly on the value of the lateral adhesion:  $\alpha_l$  ( $K_{\text{eff}} \propto \alpha_l^5$ ). For  $\Lambda_a \gg \alpha_l$ , because  $\mathcal{C}$  is quasi-linear with  $\Lambda_a$ , the bending rigidity is also roughly constant, but has a much lower value, mostly independent of  $\alpha_l$ .

Moreover, for large values of the lateral adhesion  $\alpha_l$ , the epithelium shows a discontinuous transition: The bending rigidity stays very high until a critical value of  $\Lambda_a$ .

Finally, we give a phase diagram of 3D epithelial sheet organization. There are three spinodal “tongues” and thus three critical points. For  $\gamma_b = 0$  (Fig. 4), there is a range of stability of quasi-flat sheets, around  $\Lambda_a = 0$  (squamous cells if  $\alpha_l \ll 1$ , columnar cells if  $\alpha_l \gg 1$ ). When  $\Lambda_a$  increases, the curvature of the cell sheet increases either continuously ( $\alpha_l \ll 1$ ) or discontinuously ( $\alpha_l \gg 1$ ).

**Curvature Induced by an Apical Surface Tension.** In some morphogenetic events, invagination is driven by the constriction of the entire apical cortex, instead of a circumferential apical belt (1). We set the belt tension  $\Lambda_a = 0$  and call  $\gamma_a$  the apical surface tension, which adds a contribution  $\gamma_a r_2^2$  in Eq. 4. The results are qualitatively similar to those of the previous section, although the scaling laws are different. In the regime of low apical tensions ( $\gamma_a \ll \alpha_l$ ), the curvature is  $\mathcal{C} \propto \frac{\gamma_a}{\alpha_l^5}$ . In the regime of high apical tensions ( $\gamma_a \gg \alpha_l$ ),  $r_1 \propto \gamma_a^{1/14}$ ,  $r_2 \propto \gamma_a^{-5/14}$ , and  $\mathcal{C} \propto \gamma_a^{4/7}$ . Interestingly, these two scaling laws in  $\gamma_a$  are quite different and could be distinguishable in experiments. The scaling law  $r_1 \propto r_2^{-1/5}$  also holds.

#### Cellular Tubes vs. Cellular Spheres

So far, we have calculated the spontaneous curvature of individual cells, assuming that the cell sheet would curve isotropically, with

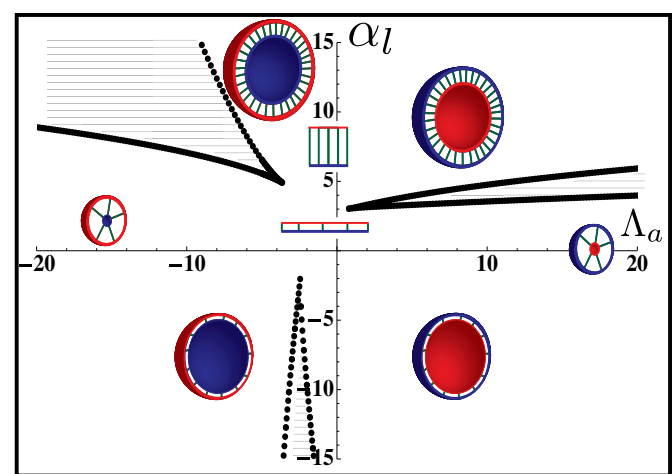


**Fig. 4.** Phase diagram of the 3D architecture of epithelial tissue, as a function of apical belt tension  $\Lambda_a$  and lateral adhesion  $\alpha_l$ , for  $\gamma_b = -1$ . The apical side is drawn in red and the basal side in blue. The apical side lines the interior of the sphere if  $\Lambda_a > 0$ , and the exterior is  $\Lambda_a > 0$ . We concentrate on the region  $\Lambda_a > 0$ : The curvature increases for increasing  $\Lambda_a$ , either continuously or discontinuously (hatched regions). The epithelium is more columnar for high values of  $\alpha_l$ .

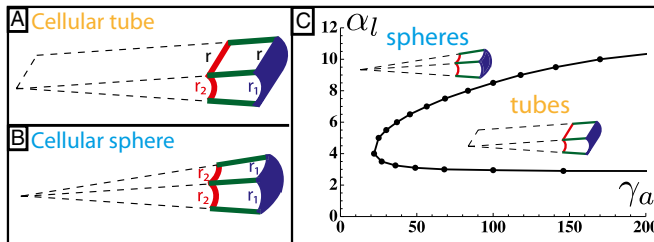


**Fig. 5.** (A and B) Comparison of the mechanical stability for cellular tubes, made of cells curved in one direction (A), and cellular spheres, curved in two directions (B). (C) Stability diagram as a function of lateral adhesion  $\alpha_l$  and apical tension  $\gamma_a$ .

a spherical geometry. Nevertheless, other geometries are seen *in vivo* and could be more stable. We now compare the stability of spheres and tubes for various parameters. A cell in a tube is curved in one direction, and we define  $r_1$  as the dimension of the apical side in the curved direction,  $r_2$  as the dimension of the basal side in the curved direction, and  $r$  as the dimension in the noncurved direction (Fig. 5 A and B).

If the apical constriction is anisotropic, as in neural tube formation, a sheet bends only in one direction, creating a tube. The anisotropy is then built into the microscopic deformation. Nevertheless, we show here that tubes could be favored even if the apical constriction is isotropic, through a spontaneous symmetry breaking at the tissue level. This is because, for a given cell volume, a tubular morphology maximizes cell-cell adhesion, because a rectangular prism has a larger surface area than a regular prism. Therefore, high values of  $\alpha_l$  tend to favor tubular geometries.

Using the same model as before, a tubular cell of volume  $V_0$  has an effective energy

$$\mathcal{F}_c = -\frac{\alpha_l}{2} \left( \frac{1}{r} + \frac{2}{r_1 + r_2} \right) + \frac{A}{4} r^2 (r_1 + r_2)^2 + \frac{A}{r_1 r_2} + \frac{A}{r} + \gamma_b r_1 r + \Lambda_a \frac{r_2 + r}{2}. \quad [7]$$

For an epithelium constricting through an apical belt, the spherical configuration is always the most stable, except at extreme values of  $\Lambda_a$ , in a very narrow parameter range. On the other hand, for an epithelium constricting through an actin cortex with apical tension  $\gamma_a$ , the range of parameters where tubes are more stable drastically widens. We compare the effective energies of the two configurations at steady state (Fig. 5C) and calculate a phase diagram as a function of  $\alpha_l$  and  $\gamma_a$ .

In the case of apical belt tension and in the limit  $\Lambda_a \gg \alpha_l$ , the scaling law of the spherical effective energy at mechanical equilibrium is  $\mathcal{F}_s \propto \Lambda_a^{4/9}$ , whereas for the cylindrical effective energy,  $\mathcal{F}_c \propto \Lambda_a^{2/3}$ , a larger exponent. This means that for large enough  $\Lambda_a$ , spheres are always more stable, which restricts drastically the stability range of tubes.

In contrast, for apical surface tension and in the regime  $\gamma_a \gg \alpha_l$ , the energies of the two configurations have the same scaling,  $\mathcal{F}_s \propto \mathcal{F}_c \propto \gamma_a^{2/7}$  (Fig. S8A), so tubular configurations have a much larger stability range. Moreover, considering a non-negligible cell-cell adhesion  $\alpha_l$  allows us to calculate the next term in the expansion of the energies:  $\mathcal{F}_c \propto \gamma_a^{2/7} - \gamma_a^{17/14} \alpha_l$  and  $\mathcal{F}_s \propto \gamma_a^{2/7} - \gamma_a^{-1/14} \alpha_l$ . When the apical tension  $\gamma_a$  increases, the cell-cell contribution stabilizes more and more the cylindrical morphology compared with the spherical. Therefore, when  $\alpha_l$  is large, cylindrical morphologies are more stable for large values of  $\gamma_a$ , as observed in the phase diagram.

Additionally, to fully explore the space of possible shapes, we consider the stability of cellular ellipsoids, made of cells that have two distinct curvatures  $C_1 = \frac{r_1 - r_2}{r_1 h}$  and  $C_2 = \frac{r_3 - r_4}{r_3 h}$  (Fig. S8B), which we calculate at mechanical equilibrium. The results confirm the previous stability diagram, the main difference being that the transition between a sphere and a tube is smooth; i.e., the stable shape is a more and more elongated ellipsoid far from the transition. For low values of  $\gamma_a$ , the ratio of the two curvatures is 1, before increasing sharply at the transition (Fig. S8C).

### Buckling Induced by Cell Shape Changes

Finally, we consider the confinement of an epithelium to an area different from its equilibrium value. If this occurs, cells can accommodate the decreased area by increasing their height. However, the area accessible to cells can also increase to its value dictated by mechanical equilibrium through an out-of-plane deformation of the entire sheet. This occurs if the energetic cost of bending the sheet is larger than the energetic cost of compression and is analogous to the Eulerian buckling of an elastic sheet under compression. For example, during *Drosophila* wing development, the columnar epithelium forms several folds. Moreover, local mutations affecting the actin belt cause the epithelium to collapse to a lower height and a bigger area and thus to form additional folds (19).

Therefore, buckling instabilities can arise not only from stresses due to cell division (34), but also from cellular shape changes, caused by adhesion or apical contractility changes. To our knowledge, this last possibility has not been explored theoretically. We therefore compare the stability of confined and buckled epithelia and consider a one-dimensional layer of columnar cells, in the limit  $\alpha_l \gg \Lambda_a$  (see SI Text for the other limit). The equilibrium base length is then  $r_0 = \frac{4}{\alpha_l}$ . Confining a cell to a new base length  $r < r_0$  costs an effective energy  $\mathcal{F}_{conf} = \frac{\alpha_l^4}{128} (\Delta r)^2$ , where  $\Delta r = r_0 - r \ll r_0$ . In a buckled sheet, parameterized by the definition  $l(z) = u \cos(qz)$  (Fig. 6), cells are forced to adopt a lampshade shape that has an energetic cost, but the amplitude and wavelength  $u$  and  $q$  are such as to accommodate cells to their equilibrium base length  $r_0 = r \left(1 + \frac{u^2 q^2}{2}\right)$ . The energetic cost of the buckled configuration for a cell (SI Text) is  $\mathcal{F}_{buck} = \frac{5 \alpha_l^7}{3} q^2 \Delta r$ . Therefore, the confinement energy depends quadratically on the confinement  $\Delta r$ , whereas the effective buckling energy is linear in  $\Delta r$ . This means that small confinements are always accommodated by a uniform squeezing of the sheet, until a critical threshold where the sheet buckles. Not surprisingly, large wavelengths ( $q \rightarrow 0$ ) are favored and reduce the buckling energy, because less bending is required of each individual cell. The

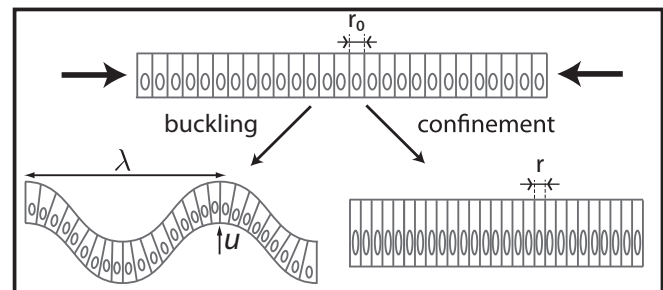


**Fig. 6.** Cell confinement and buckling. When a tissue is confined by external forces to an area lower than the area dictated by its mechanical equilibrium, it can either be homogeneously compressed or buckle to relieve the stress.

preferred wavelength is then the length of the sheet  $L$ , with a critical confinement threshold

$$\Delta r_c \propto \frac{\alpha_l^3}{L^2} \quad [8]$$

The threshold increases with  $\alpha_l$ , in agreement with our previous observation that cell–cell adhesion increases the bending rigidity of a sheet. Conversely, we consider the complementary case where the projected area of the sheet stays fixed and a mutation causes cell–cell adhesion to decrease to  $\alpha'_l = \alpha_l - \Delta\alpha_l$ . Again, the sheet buckles if the cell–cell adhesion decreases more than a threshold value  $\Delta\alpha_{lc} \propto \frac{\alpha_l^3}{L^2}$ .

## Discussion

In this article, we introduce a minimal model for epithelial cell morphology in three dimensions. Our model allows for the calculation of the equilibrium base length and height of epithelial cells as a function of three parameters: apical belt tension and cell–cell and cell–substrate tensions. These three parameters alone do not lead to stable equilibrium as soon as adhesion dominates contractile forces, and an additional term must be added to account for the fact that a cell cannot spread indefinitely. Several physical mechanisms could in principle be invoked, but the orders of magnitude we calculated suggest that the confinement energy of cytoplasmic components could be large enough to reproduce realistic aspect ratios.

It should be noted that the typical height of a squamous cell is similar to the typical radius of a columnar cell (on the order of a few microns) and that this value is comparable to the persistence length of intermediate filaments such as keratin (1  $\mu\text{m}$ ) (35), the length scale at which we expect confinement forces to be large. Therefore, the model that we propose could function as a passive size-sensing mechanism in epithelia. We insist, however, that most results presented here would not be qualitatively

different if a wide range of other stabilizing mechanisms were used, for instance a regulation of the active tensions that would function as an active size-sensing mechanism.

This theory predicts nontrivial phase transitions: On planar substrates, the aspect ratio of cells varies either continuously or discontinuously with the parameters. We give analytical criteria to discriminate between the two regimes and discuss the implications during morphogenesis. We then derive a full phase diagram of epithelial morphology in three dimensions, and a central result of this article is a scaling law for the curvature of an epithelium as a function of apical belt tension and cell–cell lateral adhesion. It is thus controlled by few parameters, which are part of a larger regulatory network. They are, in general, not varied independently *in vivo*: Both tensions and the confinement energy of the cytoskeleton could be modified as a function of cellular morphology itself. In the case of a discontinuous morphological transition, this implies protein expression levels would in turn be discontinuous.

An interesting consequence of this phase diagram is that a region exists where both columnar and squamous epithelia are stable. If cells are confined to a constant number in a constant area (Fig. S9), we thus expect a phase separation, with a region of columnar cells and a region of squamous cells, even for identical cell and substrate properties. This echoes the morphological transition of the follicle cell epithelium into two distinct populations during *Drosophila* oogenesis (28).

Our theory can also be generalized to include external stresses acting on the sheet. Additional aspects of the cell biology, such as cell division or apoptosis, or active behaviors such as migration, oscillations, and fluid pumping could be incorporated as well in a straightforward manner. Moreover, numerical simulations would be necessary to investigate the role of noise and disorder in the morphology of epithelial sheets.

1. Dawes-Hoang RE, et al. (2005) Folded gastrulation, cell shape change and the control of myosin localization. *Development* 132(18):4165–4178.
2. Montell DJ (2008) Morphogenetic cell movements: Diversity from modular mechanical properties. *Science* 322(5907):1502–1505.
3. Lecuit T, Lenne PF (2007) Cell surface mechanics and the control of cell shape, tissue patterns and morphogenesis. *Nat Rev Mol Cell Biol* 8(8):633–644.
4. Jankowski JA, Harrison RF, Perry I, Balkwill F, Tselepis C (2000) Barrett's metaplasia. *Lancet* 356(9247):2079–2085.
5. Käfer J, Hayashi T, Marée AF, Carthew RW, Graner F (2007) Cell adhesion and cortex contractility determine cell patterning in the *Drosophila* retina. *Proc Natl Acad Sci USA* 104(47):18549–18554.
6. Pouille PA, Farge E (2008) Hydrodynamic simulation of multicellular embryo invagination. *Phys Biol* 5(1):015005.
7. Hanahan D, Weinberg RA (2011) Hallmarks of cancer: The next generation. *Cell* 144(5):646–674.
8. Weber KL, Fischer RS, Fowler VM (2007) Tmod3 regulates polarized epithelial cell morphology. *J Cell Sci* 120(Pt 20):3625–3632.
9. Chauhan BK, Lou M, Zheng Y, Lang RA (2011) Balanced Rac1 and RhoA activities regulate cell shape and drive invagination morphogenesis in epithelia. *Proc Natl Acad Sci USA* 108(45):18289–18294.
10. Gelbart MA, et al. (2012) Volume conservation principle involved in cell lengthening and nucleus movement during tissue morphogenesis. *Proc Natl Acad Sci USA* 109(47):19298–19303.
11. Zihler P, Krajnc M, Storgel N, Brezavsek AH (2013) A tension-based model of flat and corrugated simple epithelia. *Soft Matter* 9(34):8368–8377.
12. Hočevá Brezavšček A, Rauzi M, Leptin M, Zihler P (2012) A model of epithelial invagination driven by collective mechanics of identical cells. *Biophys J* 103(5):1069–1077.
13. Hilgenfeldt S, Erisken S, Carthew RW (2008) Physical modeling of cell geometric order in an epithelial tissue. *Proc Natl Acad Sci USA* 105(3):907–911.
14. Farhadifar R, Röper JC, Aigouy B, Eaton S, Jülicher F (2007) The influence of cell mechanics, cell–cell interactions, and proliferation on epithelial packing. *Curr Biol* 17(24):2095–2104.
15. Gibson MC, Patel AB, Nagpal R, Perrimon N (2006) The emergence of geometric order in proliferating metazoan epithelia. *Nature* 442(7106):1038–1041.
16. Osterfield M, Du X, Schüpbach T, Wieschaus E, Shvartsman SY (2013) Three-dimensional epithelial morphogenesis in the developing *Drosophila* egg. *Dev Cell* 24(4):400–410.
17. Gomez JM, Wang Y, Riechmann V (2012) Tao controls epithelial morphogenesis by promoting Fasciclin 2 endocytosis. *J Cell Biol* 199(7):1131–1143.
18. Melani M, Simpson KJ, Brugge JS, Montell D (2008) Regulation of cell adhesion and collective cell migration by hindsight and its human homolog RREB1. *Curr Biol* 18(7):532–537.
19. Widmann TJ, Dahmann C (2009) Dpp signaling promotes the cuboidal-to-columnar shape transition of *Drosophila* wing disc epithelia by regulating Rho1. *J Cell Sci* 122(Pt 9):1362–1373.
20. Manning ML, Foty RA, Steinberg MS, Schoetz EM (2010) Coaction of intercellular adhesion and cortical tension specifies tissue surface tension. *Proc Natl Acad Sci USA* 107(28):12517–12522.
21. Ingber DE, Prusty D, Sun Z, Betensky H, Wang N (1995) Cell shape, cytoskeletal mechanics, and cell cycle control in angiogenesis. *J Biomech* 28(12):1471–1484.
22. Coulombe PA, Wong P (2004) Cytoplasmic intermediate filaments revealed as dynamic and multipurpose scaffolds. *Nat Cell Biol* 6(8):699–706.
23. Versaevel M, Grevese T, Gabriele S (2012) Spatial coordination between cell and nuclear shape within micropatterned endothelial cells. *Nat Commun* 3:671.
24. de Gennes P-G (1979) *Scaling Concepts in Polymer Physics* (Cornell Univ Press, Ithaca, NY).
25. Claessens MMAE, Tharmann R, Kroy K, Bausch AR (2006) Microstructure and viscoelasticity of confined semiflexible polymer networks. *Nat Phys* 2(3):186–189.
26. Valentine MT, Perlman ZE, Mitchison TJ, Weitz DA (2005) Mechanical properties of *Xenopus* egg cytoplasmic extracts. *Biophys J* 88(1):680–689.
27. Maître JL, et al. (2012) Adhesion functions in cell sorting by mechanically coupling the cortices of adhering cells. *Science* 338(6104):253–256.
28. Kolahi KS, et al. (2009) Quantitative analysis of epithelial morphogenesis in *Drosophila* oogenesis: New insights based on morphometric analysis and mechanical modeling. *Dev Biol* 331(2):129–139.
29. Solon J, Kaya-Copur A, Colombelli J, Brunner D (2009) Pulsed forces timed by a ratchet-like mechanism drive directed tissue movement during dorsal closure. *Cell* 137(7):1331–1342.
30. Saez A, et al. (2010) Traction forces exerted by epithelial cell sheets. *J Phys Condens Matter* 22(19):194119.
31. Zhang J, et al. (2005) Actin at cell–cell junctions is composed of two dynamic and functional populations. *J Cell Sci* 118(Pt 23):5549–5562.
32. Israelachvili JN, Mitchell DJ, Ninham BW (1976) Theory of self-assembly of hydrocarbon amphiphiles into micelles and bilayers. *J Chem Soc Faraday Trans II* 72: 1525–1568.
33. Harris AR, et al. (2012) Characterizing the mechanics of cultured cell monolayers. *Proc Natl Acad Sci USA* 109(41):16449–16454.
34. Hannezo E, Prost J, Joanny JF (2011) Instabilities of monolayered epithelia: Shape and structure of villi and crypts. *Phys Rev Lett* 107(7):078104.
35. Mücke N, et al. (2004) Assessing the flexibility of intermediate filaments by atomic force microscopy. *J Mol Biol* 335(5):1241–1250.

# Supporting Information

Hannezo et al. 10.1073/pnas.1312076111

## SI Text

### Morphologies of Planar Epithelial Cells

**Derivation of the Effective Energy.** For an hexagonal prism,  $V = \frac{\sqrt{3}}{2}r^2h$ ,  $\mathcal{A}_{\text{basal}} = \frac{\sqrt{3}}{2}r^2$ ,  $\mathcal{A}_{\text{lat}} = 2\sqrt{3}rh$ , and  $\mathcal{P}_{\text{ap}} = 2\sqrt{3}r$ . The total effective energy is then

$$\begin{aligned} F = & \gamma_b \frac{\sqrt{3}}{2}r^2 - \alpha_l 2\sqrt{3}rh + 2\sqrt{3}\Lambda_a r + \frac{K}{2} \left( \frac{\sqrt{3}}{2}r^2h - V_0 \right)^2 \\ & + \frac{A}{h^2} + \frac{2A}{r^2}. \end{aligned} \quad [\text{S1}]$$

or, if the volume is constant ( $V = V_0$ ),

$$F = \gamma_b \frac{\sqrt{3}}{2}r^2 - 4\alpha_l \frac{V_0}{r} + 2\sqrt{3}\Lambda_a r + \frac{4Ar^4}{3V_0^2} + \frac{2A}{r^2}. \quad [\text{S2}]$$

Choosing  $V_0^{1/3}$  as the unit length and  $\frac{A}{V_0^{2/3}}$  as the unit energy, we obtain a dimensionless energy with only three effective parameters. Using nondimensional variables that we rename as  $\frac{r}{(4/3)^{1/6}V_0^{1/3}} \rightarrow r$  and  $\frac{\mathcal{F}V_0^{3/2}}{(3/4)^{1/3}A} \rightarrow \mathcal{F}$ ,

$$\mathcal{F} = \frac{\gamma_b V_0^{4/3}}{A} r^2 - \frac{\alpha_l}{AV_0^{2/3}r} + \frac{\Lambda_a V_0}{A} r + r^4 + \frac{2}{r^2}. \quad [\text{S3}]$$

And from the rescaling in the main text,

$$\mathcal{F} = \gamma_b r^2 - \frac{\alpha_l}{r} + \Lambda_a r + r^4 + \frac{2}{r^2}. \quad [\text{S4}]$$

**Force Balance on a Cell.** We first write the force balance in the vertical direction (Fig. S1), on the apical surface. The compressibility of the cell creates a pressure  $K(V - V_0)$ , so

$$\frac{2A}{h^3} - \alpha_l \mathcal{P}_{\text{ap}} + K(V - V_0) \mathcal{A}_{\text{apical}} = 0, \quad [\text{S5}]$$

which is equivalent to  $\frac{d\mathcal{F}}{dh} = 0$ .

We now write the force balance in the radial direction, on a lateral face of the prism:

$$\frac{4A}{r^3} - 2 \cos\left(\frac{\pi}{6}\right) \Lambda_a - \frac{\sqrt{3}r}{2} \gamma_b + K(V - V_0) \mathcal{A}_{\text{lat}} = 0, \quad [\text{S6}]$$

which again is equivalent to  $\frac{d\mathcal{F}}{dr} = 0$ .

**Orders of Magnitude.** Ref. 1 studies the confinement of actin fibers of physiological concentrations in emulsion droplets of radii varying between 5  $\mu\text{m}$  and 50  $\mu\text{m}$ . Because actin filaments have a persistence length of around 15  $\mu\text{m}$ , confinement effects occur around these length scales and are monitored through micro-rheological measurements of the Plateau modulus  $G_0$ . This Plateau modulus is thus roughly constant for large sizes, before increasing drastically with confinement. The average value at the

onset of confinement is of order  $G_0 = 0.2$  Pa, which fixes an energy scale, for a cell of volume  $V_0 \approx 10^{-15}\text{m}^3$  (2), of  $G_0 V_0 = 2.10^{-16}$  J. This corresponds to a force of 1 nN exerted on a length scale of 200 nm, not far from the values forces exerted by cytoskeletal filament bundles in a cell.

Because the energy scale in our model is  $\frac{A}{V_0^{2/3}}$ , we make a rough estimation  $A \approx 10^{-24} \text{ J} \cdot \text{m}^2$  in the main text.

Ref. 3 studies the rheology of *Xenopus* egg cytoplasmic extracts, which contain actin, microtubules, and intermediate filaments. Moreover, the extracts remains metabolically active, with reserves of ATP, and thus quite close to physiological conditions. The extract is shown to behave like a viscoelastic solid over timescales of several hours. The moduli measured are in the range 2 – 10 Pa, always higher than that of the loss modulus, and therefore one order of magnitude larger than the moduli of actin filaments alone. Therefore, we estimated in the main text  $A \approx 10^{-24} - 10^{-23} \text{ J} \cdot \text{m}^2$ .

Obviously, the mammalian epithelial cell is a more complex material. In particular, filaments can be bundled and aligned actively in vivo, which would decrease the energy necessary for confinement. In our model, this would translate to a homothetic increase of our parameters  $\gamma_b$ ,  $\alpha_l$ , and  $\Lambda_a$ . One could imagine a biochemical feedback of the nucleus compression on the values of the tensions, which could be hinted by experiments such as ref. 4, showing that a mechanical compression of the nucleus in endothelial cells caused a compaction of chromatin.

All these remarks reinforce the pertinence of drawing phase diagrams of cellular morphology: Although biological tissues can take not trivial paths on these phase diagrams, they are still bound to them, and the qualitative results we describe apply.

**Critical Point.** A critical point, defined as  $\frac{d\mathcal{F}}{dr} = \frac{d^2\mathcal{F}}{dr^2} = \frac{d^3\mathcal{F}}{dr^3} = 0$  (where two spinodals meet), separates regions of continuous and discontinuous morphological transitions. It is possible to get analytical limits for the coordinates of the critical point. If  $\alpha_l \ll -1$ , then the lateral tension is enough to stabilize cells to a nonzero base length, and the term  $\frac{1}{r^2}$  in the energy becomes negligible. The condition  $\frac{d\mathcal{F}}{dr} = \frac{d^2\mathcal{F}}{dr^2} = 0$  can then be written as

$$2\gamma_b r + \frac{\alpha_l}{r^2} + \Lambda_a + 4r^3 = 0 \quad [\text{S7}]$$

$$2\gamma_b - \frac{2\alpha_l}{r^3} + 12r^2 = 0. \quad [\text{S8}]$$

As long as  $\gamma_b < 0$  and  $|\gamma_b| \gg 1$ , there are two clear limits to Eq. S8:  $r = \sqrt{\frac{-\gamma_b}{6}}$  and  $r = \left(\frac{\alpha_l}{-\gamma_b}\right)^{1/3}$ , which, respectively, yield in the  $(\alpha_l, \Lambda_a)$  plane  $\Lambda_a = \frac{4}{3\sqrt{6}}(-\gamma_b)^{3/2}$  and  $\alpha_l = \frac{\Lambda_a^3}{27\gamma_b^2}$ . One can check that this is indeed a good approximation of the numerical solution (Fig. S4).

Moreover, the condition  $\frac{d^3\mathcal{F}}{dr^3} = 0$ , under this approximation, leads to  $r = \left(\frac{4}{\alpha_l}\right)^{1/5}$ , and at the critical point,  $\alpha_{lc} = \frac{1}{25\sqrt{10}}(-\gamma_b)^{5/2}$  and  $\Lambda_{ac} = \sqrt{\frac{2}{5}}(-\gamma_b)^{3/2}$ .

**Cell Confinement and Phase Separation.** We come back to the question of a tissue confined on a rigid substrate, with no division or apoptosis, for which no buckling is allowed. Considering  $N$

identical cells and a total area  $A_0$ , there are no degrees of freedom:  $r^2 = \frac{A_0}{N} = r_0^2$ . The total energy of the layer is then

$$\mathcal{E} = N\mathcal{F}(r_0). \quad [\text{S9}]$$

Nevertheless, we have seen that our mechanical equations lead to two possible cell aspect ratios. Therefore, the cells can minimize their total energy by phase separating into  $N_c$  columnar cells of area  $r_c^2$  and  $N_s$  squamous cells of area  $r_s$ , such that  $N = N_s + N_c$  and  $A_0 = N_s r_s^2 + N_c r_c^2$ . We define  $n_s = \frac{N_s}{N}$  and  $n_c = \frac{N_c}{N}$  as the fractions of squamous and columnar cells and  $a_0 = \frac{A_0}{N}$  as the average area accessible per cell.

The total energy is then

$$\mathcal{E} = N \left( n_s \mathcal{F}(r_s) + (1 - n_s) \mathcal{F} \left( \frac{a_0 - n_s r_s^2}{1 - n_s} \right) \right). \quad [\text{S10}]$$

We minimize the energy from Eq. S10 with respect to the two independent parameters  $r_s$  and  $n_s$  while varying the single relevant control parameter,  $a_0$ . In this problem,  $\gamma_b$  drops out of the total energy, because the basal area is constant. On the other hand,  $\Lambda_a$  and  $\alpha_l$  control the onset of phase separation of the cells. As analyzed previously, high values of either  $\Lambda_a$  or  $\alpha_l$  favor a bistable equilibrium. When squamous cells are more and more confined, their area uniformly decreases until a phase separation threshold, after which a mixture of columnar and squamous cells coexists (Fig. S9A). Additional confinement does not change the morphology of either type of cell. Instead, the sheet accommodates the decreased area by converting squamous cells into columnar cells (a numerical calculation is given in Fig. S9B). For very high confinements, only columnar cells remain and are progressively squeezed additionally toward more and more columnar aspect ratios. For low values of  $\Lambda_a$  or  $\alpha_l$ , no phase separation occurs, and the morphological transition is instead smooth (Fig. S9C). We numerically compute a phase diagram showing the region of phase separation (Fig. S9D).

### Epithelial Sheet Bending

**Derivation of the Energy for Tubes and Spheres.** In the case of a cell curved in two directions (forming a sphere), we define the height  $h$  of a cell (we consider a cell as a section of a shell, so that the distance between apical and basal sides is  $h$  everywhere; Fig. S5), the side length of the apical surface  $r_1$ , and the side length of the basal surface  $r_2$ . To calculate the confinement energy of a columnar curved cell, we parameterize the characteristic radius of a cell at a height  $z$  as  $r(z) = r_1 + \frac{r_2 - r_1}{h} z$ . We integrate the confinement energy of slices of thickness  $dz$ :

$$\mathcal{E}_c = \frac{1}{h} \int_0^h \frac{2}{r(z)^2} dz = \frac{2}{r_1 r_2}. \quad [\text{S11}]$$

The confinement energy for the curved cell is thus approximately  $\mathcal{E}_{conf} = \frac{1}{h^2} + \frac{2}{r_1 r_2}$ . Moreover, the lateral area is then  $h \frac{r_1 + r_2}{2}$ , the volume is  $h \frac{r_1^2 + r_2^2 + r_1 r_2}{3}$ , and the total energy for a cell is

$$\mathcal{F}_s = \frac{A}{h^2} + 2 \frac{A}{r_1 r_2} - \alpha_l h \frac{r_1 + r_2}{2} + \gamma_b r_1^2 + \Lambda_a r_2 + K \left( h \frac{r_1^2 + r_2^2 + r_1 r_2}{3} - V_0 \right). \quad [\text{S12}]$$

If the cell volume is constant,

$$\begin{aligned} \mathcal{F}_s = & -\frac{3\alpha_l}{2} \frac{r_1 + r_2}{r_1^2 + r_2^2 + r_1 r_2} + \frac{A}{9} (r_1^2 + r_2^2 + r_1 r_2)^2 + \frac{2A}{r_1 r_2} \\ & + \gamma_b r_1^2 + \Lambda_a r_2. \end{aligned} \quad [\text{S13}]$$

For a cell curved in one direction (forming a tube), the perimeter of the apical side is  $\frac{r_1 + r_2}{2}$ , the basal area is  $r_1 r_2$ , the lateral area is  $h(\frac{r_1 + r_2}{2})$ , and the volume is  $h r_1 r_2$ . The same calculation for the confinement energy yields a contribution  $\frac{1}{r_1 r_2}$  in the curved direction and  $\frac{1}{r_2^2}$  in the uncurved direction. The total energy is then

$$\begin{aligned} \mathcal{F}_c = & -\frac{\alpha_l}{2} \left( \frac{1}{r} + \frac{2}{r_1 + r_2} \right) + \frac{A}{4} r^2 (r_1 + r_2)^2 + \frac{A}{r_1 r_2} + \frac{A}{r^2} \\ & + \gamma_b r_1 r_2 + \Lambda_a \frac{r_1 + r_2}{2}. \end{aligned} \quad [\text{S14}]$$

In the case of an apical belt tension, and in the limit  $\Lambda_a \gg \alpha_l$ , the energies of the spherical and cylindrical morphologies  $F_s$  and  $F_c$  are

$$F_s \approx \frac{2}{r_1 r_2} + \frac{r_1^4}{9} + \Lambda_a r_2 \quad [\text{S15}]$$

$$F_c \approx \frac{1}{r_1 r_2} + \frac{1}{r^2} + \frac{r_1^2 r^2}{4} + \Lambda_a \frac{r + r_2}{2}. \quad [\text{S16}]$$

Minimizing each energy with respect to  $r_1, r_2$  or  $r_1, r_2, r$ , the scaling of the spherical energy at equilibrium is  $F_s \propto \Lambda_a^{4/9}$ , whereas that of the cylindrical energy is  $F_c \propto \Lambda_a^{2/3}$ , in agreement with numerical integrations (Fig. S8A).

**Finite Elasticity of the Substrate.** In the previous sections, we analyzed two limiting cases of infinitely rigid substrate (planar sheets) and infinitely soft substrate (bended sheets). In general, however, the underlying substrate has a finite elasticity. In many events of epithelial sheet bending, the sheet rests on a thin placode (5). We model the substrate with a bending modulus  $K_p$ . This adds a new contribution to the energy (6), proportional to the basal area of a cell  $r_1^2$ :

$$F_{bend} = \left( \frac{K_p}{2} C^2 \right) r_1^2. \quad [\text{S17}]$$

The two limiting cases studied in the main text are  $K_p \rightarrow \infty$  and  $K_p \rightarrow 0$ .

Of course, increasing the bending modulus of the stroma always decreases the spontaneous curvature of the epithelium. Fig. S6B displays a numerical integration for the same set of parameters as before:  $\gamma_b = 0$ ,  $\alpha_l = 4.5$ , and  $\Lambda_a = 10$ . Defining an effective bending modulus  $K_{eff}$  resisting the apical constriction, we find that  $K_{eff}$  is the sum of the effective modulus of the sheet described previously and the bending modulus of the stroma, as expected by putting two sheets in parallel:  $K_{eff} = K_p + K_{sheet}$ , where  $K_{sheet} = \frac{\Lambda_a}{C}$ , given in Eq. 6 of the main text. Therefore,  $K_{eff} \rightarrow K_p$ , when  $K_p \rightarrow \infty$ , as expected, and  $K_{eff}$  converges to the same constant  $K_{sheet}$  as before when  $K_p \rightarrow 0$ . When exploring the full parameter space ( $\gamma_b \neq 0$ ), we find additional complex behaviors (Fig. S6C).

**Influence of the Cell–Substrate Tension  $\gamma_b$  on the Phase Diagram.** We now consider the alternative case of an invagination driven by basal spreading ( $\gamma_b \neq 0$  and  $\Lambda_a \approx 0$ ). The topology of the phase

diagram (Fig. S7B) is different. Basal adhesion favors curved morphologies, lowering the effective bending stiffness of the sheet. As before, we derive scaling laws for large values of the basal adhesion ( $\gamma_b < 0$  and  $|\gamma_b| \gg \alpha_l$ ):  $r_1 \propto \sqrt{-\gamma_b}$ ,  $r_2 \propto -\gamma_b^{-1}$ , and

$$\mathcal{C} \propto (-\gamma_b)^{5/2}. \quad [\text{S18}]$$

We now consider both apical belt tension and basal spreading. In the main text, we produce a phase diagram of 3D epithelial sheet morphology (Fig. S7).

For  $\gamma_b = 0$  (Fig. S7A and B), there is a zone of stability of quasi-flat sheets, around  $\Lambda_a = 0$ . These are sheets of squamous cells if  $\alpha_l \ll 1$  and sheets of columnar cells if  $\alpha_l \gg 1$  with a continuous transition between the two. When  $\Lambda_a$  increases, the spontaneous curvature of the epithelial sheet increases either continuously ( $\alpha_l \ll 1$ ) or discontinuously ( $\alpha_l \gg 1$ ), as we discuss in the main text.

When  $\gamma_b$  increases, this destabilizes flat sheets and causes the regions of stability of curved epithelial tissues to invade the phase diagram. A complex phase transition occurs: Two critical points first merge, and a region with three stable morphologies appears, when the third critical point merges with the other spinodals.

**Sign of the Epithelial Curvature.** In our model, the sign of the epithelial curvature can be either positive or negative. This depends on the relative values of the apical belt tension  $\Lambda_a$  and the basal tension  $\gamma_b$ .

To quantify this effect, we perform a numerical integration of the phase diagram of 3D architecture in the  $\Lambda_a, \gamma_b$  plane (Fig. S5A). We plot both the spinodal lines delimiting bi-stable equilibria regions and the line separating positive and negative curvatures. This separation is defined by the conditions  $\frac{\partial \mathcal{F}}{\partial r_1} = \frac{\partial \mathcal{F}}{\partial r_2} = 0$  and  $r_1 = r_2$ .

As we show in Fig. S5B, the separation depends on the cell–cell lateral adhesion  $\alpha_l$ . As  $\alpha_l$  increases, the region of stability of negative curvatures shrinks.

For  $\Lambda_a$  and  $\gamma_b$  both positive, the confinement term  $\frac{1}{h^2}$  is not needed to stabilize the shapes. Neglecting it, we can calculate analytically the separation line between positive and negative curvatures, which satisfies the equation

$$\alpha_l = 8 \frac{\gamma_b}{\Lambda_a} - \frac{\Lambda_a^3}{2\gamma_b^2} \leq. \quad [\text{S19}]$$

This shows that indeed the solution  $\alpha_l$  decreases monotonously with increasing  $\Lambda_a$  and increases monotonously with increasing  $\gamma_b$ . Moreover, on the zero-curvature line,  $r_1 = r_2 = \frac{\Lambda_a}{2\gamma_b}$ .

We also show a numerical solution for the basal and apical lengths for increasing apical belt tension  $\Lambda_a$ , for a given set of parameters (Fig. S5C).

Interestingly, studies on gastrulation in *Drosophila* (7) have shown that the transition from a concave to a convex epithelium is mediated by a relocalization of myosins from the basal side of the mesoderm to the apical side. In our formalism, this would mean that  $\Lambda_a$  increases as  $\gamma_b$  decreases.

Alternatively, if we consider an apical surface tension  $\gamma_a$  instead of an apical belt tension  $\Lambda_a$ , then our model is rigorously up–down symmetric, i.e., upon the substitution ( $r_1 \rightarrow r_2$ ,  $\gamma_b \rightarrow \gamma_a$ ). Then, the criterion for positive curvature is simply  $\gamma_a > \gamma_b$  and for negative curvature is  $\gamma_a < \gamma_b$ .

**Stability of Cellular Ellipsoid.** We write, in analogy with the previous sections, the energy of a cell pictured in Fig. S8B, i.e., curved in two directions with two different curvatures  $\mathcal{C}_1 = \frac{r_1 - r_2}{r_2 h}$  and

$\mathcal{C}_2 = \frac{r_3 - r_4}{r_3 h}$ . The volume of such a cell is  $V = h \frac{2r_1 r_3 + r_2 r_3 + r_1 r_4 + 2r_2 r_4}{6}$ , and the energy is

$$\begin{aligned} \mathcal{F}_e = & \frac{1}{h^2} + \frac{1}{r_1 r_2} + \frac{1}{r_3 r_4} - \alpha_l h \frac{1}{2} \left( \frac{r_1 + r_2}{2} + \frac{r_3 + r_4}{2} \right) \\ & + \gamma_b r_1 r_3 + \gamma_a r_2 r_4 + K(V-1)^2. \end{aligned} \quad [\text{S20}]$$

If the cell volume is constant,

$$\begin{aligned} \mathcal{F}_e = & \left( \frac{2r_1 r_3 + r_2 r_3 + r_1 r_4 + 2r_2 r_4}{6} \right)^2 + \frac{A}{r_1 r_2} + \frac{A}{r_3 r_4} \\ & - \frac{3\alpha_l}{2r_1 r_3 + r_2 r_3 + r_1 r_4 + 2r_2 r_4} \left( \frac{r_1 + r_2}{2} + \frac{r_3 + r_4}{2} \right) \\ & + \gamma_b r_1 r_3 + \gamma_a r_2 r_4. \end{aligned} \quad [\text{S21}]$$

We confirm the stability analysis of cellular spheres vs. cellular tubes. The main difference is that the transition is no longer sharp, with a pitchfork supercritical bifurcation between a sphere (where the two curvatures are equal) and an elongated ellipsoid that approaches a tube (Fig. S8C). Nevertheless, infinite tubes are never stable in this model, because there is always a small curvature in the longitudinal direction.

**Buckling Induced by Cell Shape Changes.** As indicated in the main text, we parameterize the out-of-plane deformation of a buckled cell sheet by  $l(z) = u \cos(qz)$ , and the amplitude and wavelength  $u$  and  $q$  are such as to accommodate cells to their equilibrium height  $h_0$  and average base length

$$r_0 = r \left( 1 + \frac{u^2 q^2}{2} \right) \quad [\text{S22}]$$

in the regime of small curvatures  $uq \ll 1$ .

Nevertheless, in the buckled state, each cell is forced to adopt a spontaneous curvature, which is on average  $\mathcal{C}_{\text{sheet}} = uq^2$  and has an energetic cost.

Therefore, one should compare the energetic cost of buckling and the energetic cost of cells not adopting their preferred height.

We define  $\delta r$  such that the elongated base length of a cell is  $r_0 + \delta r$  and the shortened base length of a cell is  $r_0 - \delta r$ . The spontaneous curvature of a cell is  $\mathcal{C}_{\text{cell}} = r_0 \delta r$  and has to be equal to the mean curvature of a sheet  $\mathcal{C}_{\text{sheet}}$ .

Combined with Eq. S22, this yields a relationship between the confinement  $\Delta r = r_0 - r$  and the cell deformation  $\delta r$ :

$$\delta r = \sqrt{\frac{\alpha_l^3 \Delta r}{32}} q. \quad [\text{S23}]$$

The energetic cost in the buckled configuration can then be deduced from Eq. S14, with  $r_1 = r_0 + \delta r$  and  $r_2 = r_0 - \delta r$ :

$$\mathcal{F}_{\text{buck}} = \frac{5}{3} \frac{\alpha_l^7}{4^6} q^2 \Delta r. \quad [\text{S24}]$$

**Scaling Laws for a Generic Hard-Core Repulsion.** We consider a more generic stabilizing energy of cytoskeleton confinement (or membrane confinement),  $\mathcal{E}_{\text{repuls}} = \frac{1}{h^n} + \frac{2}{r^p} = r^{2n} + \frac{2}{r^p}$ , to show that our qualitative results are unaffected by the assumption  $n=2$  we made in the main text.

We start by cells on rigid substrates. If cell–cell adhesion and actin belt contractility are small ( $\alpha_l, \Lambda_a \ll |\gamma_b|$ ), cells are squamous

and spread to a base length  $r \approx \left(\frac{\gamma_b}{n}\right)^{1/(2n-2)} \gg 1$ . If cell-cell adhesion is dominant ( $\alpha_l \gg 1$ ,  $|\gamma_b| \approx 0$ ), cells are columnar and the stable base length is  $r \approx \left(\frac{\alpha_l}{\Lambda_a}\right)^{1/(n-1)} \ll 1$ . If the apical belt is dominant ( $\Lambda_a \gg 1$  and  $\alpha_l \approx 0$ ), cells are columnar and the stable base length is  $r \approx \left(\frac{2n}{\Lambda_a}\right)^{1/(n+1)} \ll 1$ .

We plot in Fig. S2A the phase diagram of epithelial morphologies on flat substrates for various values of  $n$ , which we have chosen to correspond to various assumptions on the nature of confined polymers, to show that it still has the same topology.

In three dimensions, the scaling laws for the spontaneous curvature in the low  $\Lambda_a$ , high  $\alpha_l$  regimes are not affected. Indeed, for any  $n$ , the scaling law for the spontaneous curvature is

$$C \propto \frac{\Lambda_a}{\alpha_l^4 - 4n\alpha_l^{2n-1}}, \quad [S25]$$

and for any  $n > 1$ , in the limit  $\alpha_l \gg 1$ ,  $\alpha_l^4 \gg \alpha_l^{2n-1}$ . For the same reason, the scaling law for a small apical constriction is not affected. On the other hand, for an apical belt tension, in the high  $\Lambda_a$  regime,

$$C \propto \Lambda_a^{\frac{8}{2n+5}}, \quad [S26]$$

and for an apical surface tension, in the high  $\gamma_a$  regime,

$$C \propto \gamma_a^{\frac{4}{2n+5}}. \quad [S27]$$

Again, we show the phase diagram of curved epithelia for a different value of  $n$ , to demonstrate that the main features remain unchanged. For  $n=4$  (Fig. S2B), there are still three spinodal tongues in the phase diagram for  $\gamma_b=0$ , which merge for increasing values of  $\gamma_b$ .

We also plot for  $n=4$  the phase diagram of the stability of tubes vs. spheres, which again is not changed qualitatively (Fig. S2C).

Finally, even for these high-constriction regimes, there are some scaling laws that are completely generic. Notably, in both cases of belt tension and surface tension, the scaling law

$$r_1 \propto r_2^{-1/5} \quad [S28]$$

holds for any  $n$ , which is again a strong prediction that could be tested experimentally.

**Discussion of Different Hypotheses for the Stabilization of Cell Shape.** In the main text, we proposed that the confinement of cytoplasmic components could be a mechanical cue that determines the morphology of epithelial cells, in concert with the active surface tensions from the apical, lateral, and basal sides. Obviously, alternative mechanisms of stabilization would be imaginable, for instance the active regulation of tensions to approach a target cellular shape, as discussed in ref. 8.

1. Claessens MMAE, Tharmann R, Kroy K, Bausch AR (2006) Microstructure and viscoelasticity of confined semiflexible polymer networks. *Nat Phys* 2(3):186–189.
2. Kolahi KS, et al. (2009) Quantitative analysis of epithelial morphogenesis in Drosophila oogenesis: New insights based on morphometric analysis and mechanical modeling. *Dev Biol* 331(2):129–139.
3. Valentine MT, Perlman ZE, Mitchison TJ, Weitz DA (2005) Mechanical properties of Xenopus egg cytoplasmic extracts. *Biophys J* 88(1):680–689.
4. Versaevel M, Grevesse T, Gabriele S (2012) Spatial coordination between cell and nuclear shape within micropatterned endothelial cells. *Nat Commun* 3:671.

On flat substrates, we assume that cells have a preferred lateral area  $A_l^0$  and a basal area  $A_b^0$ , and we expand the lateral and basal tensions, respectively, around these preferred areas:

$$\gamma_b = \gamma_b^0 + \delta_1 (r^2 - A_b^0) \quad [S29]$$

$$\alpha_l = \alpha_l^0 - \delta_2 \left( \frac{V_0}{r} - A_l^0 \right). \quad [S30]$$

If  $\delta_1$  and  $\delta_2$  are positive, then the system is stable, and these stabilizing terms are exactly the same from a mathematical point of view as the ones described in the main text. The previous analysis then holds unchanged. In particular, this type of stabilizing mechanism gives rise to the same type of continuous vs. discontinuous transitions in cellular aspect ratios.

If  $\delta_1$  or  $\delta_2$  is negative, then the system is linearly unstable: One must expand the tensions up to the next order. Additional stable states are generically expected in this case.

For curved epithelia, the number of possible stabilizing terms is much larger. We fix  $\gamma_b=0$  in analogy to that in the main text, and we assume, as an example, an active regulation of the lateral adhesion  $\alpha_l$ .

In analogy with the previous equations, we write the simplest dependence of  $\alpha_l$  on  $A_{ap}$  and  $A_{bas}$ , which avoids  $A_{bas}=r_1^2 \rightarrow 0$  and  $A_{ap}=r_2^2 \rightarrow 0$ ,

$$\alpha_l = \alpha_l^0 - \delta_3 \left( \frac{1}{A_{ap}} + \frac{1}{A_{bas}} \right), \quad [S31]$$

and we incorporate, as in the main text, a term in  $\frac{4}{h^2}$  in the energy to avoid  $r_1 \rightarrow \infty$ . We show that the main features of 3D architecture discussed in the main text are preserved using this assumption. Indeed, for low values of  $\alpha_l$ , the curvature modulus of the sheet is low and the curvature increases smoothly with  $\Lambda_a$ . Moreover,  $\alpha_l$  increases with increasing  $\Lambda_a$  (Fig. S3A). Above a critical value of  $\alpha_l$ , the curvature modulus remains high until a critical value of  $\Lambda_a$ , above which it jumps to lower values. Interestingly,  $\alpha_l$  undergoes the same type of continuous vs. discontinuous transitions as the geometrical parameters  $r_1$  and  $r_2$ .

The phase diagram of epithelial cell morphology in 3D (Fig. S3B) is also similar to the one in the main text, with three spinodals joining for increasing values of  $\gamma_b$ . On the other hand, in this model, spheres are always favored compared with tubes, which may be related to the fact the effective lateral adhesion is lowered considerably (Fig. S3A) as  $\Lambda_a$  increases and  $r_2$  decreases ( $\alpha_l$  is always positive for large enough  $\Lambda_a$ ; therefore, the hypothesis underlying the qualitative argument of the main text for tubular stability does not hold).

Experiments would be needed to verify whether the cellular morphology (for instance, the value of the apical and basal areas) has indeed a feedback effect on tensions.

5. Borges RM, Lamers ML, Forti FL, Santos MFD, Yan CYI (2011) Rho signaling pathway and apical constriction in the early lens placode. *Genesis* 49(5):368–379.
6. Landau L, Lifchitz E (1970) *Theory of Elasticity, A Course of Theoretical Physics* (Pergamon, Oxford), Vol 7.
7. Dawes-Hoang RE, et al. (2005) Folded gastrulation, cell shape change and the control of myosin localization. *Development* 132(18):4165–4178.
8. Manning ML, Fofy RA, Steinberg MS, Schoetz EM (2010) Coaction of intercellular adhesion and cortical tension specifies tissue surface tension. *Proc Natl Acad Sci USA* 107(28):12517–12522.

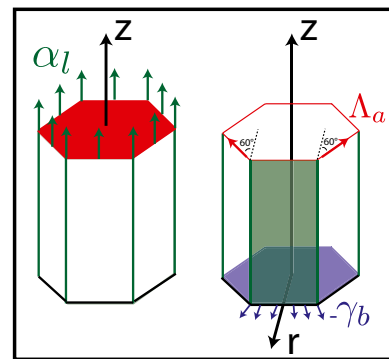


**Fig. S1.** Force balance on a cell.

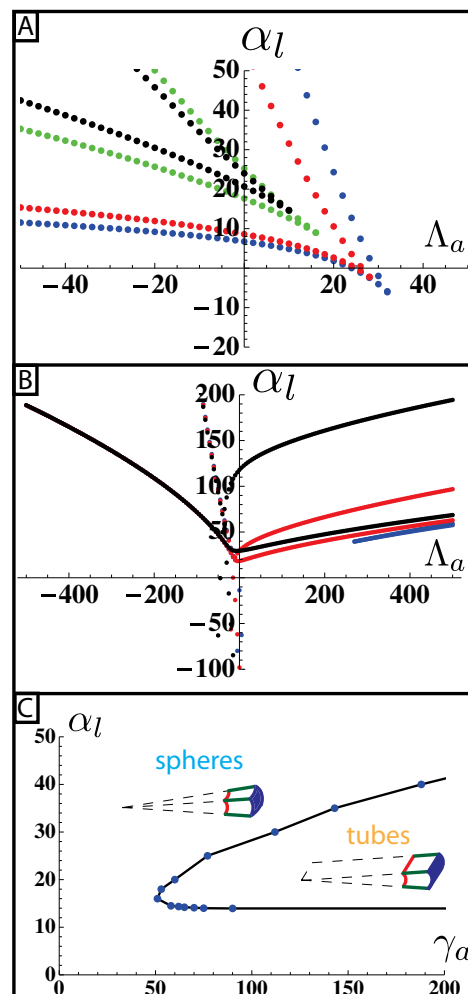


**Fig. S2.** Phase diagrams for various values of the exponent  $n$  of polymer repulsion. (A) Phase diagram of the 2D architecture of epithelial tissue on planar substrates, as a function of apical belt tension  $\Lambda_a$  and cell-cell adhesion  $\alpha_l$ , for  $\gamma_b = 15$  and  $n = 2$  (blue),  $n = 9/4$  (red),  $n = 7/2$  (green), and  $n = 4$  (black). (B) Evolution of the phase diagram of the 3D architecture of curved epithelia for  $n = 4$  and for various values of  $\gamma_b = 1$  (blue),  $\gamma_b = 6$  (red), and  $\gamma_b = 15$  (black). (C) Phase diagram of tubular vs. spherical organization of curved tissue, as a function of apical surface tension  $\gamma_a$  and cell-cell adhesion  $\alpha_l$ , for  $n = 4$ .

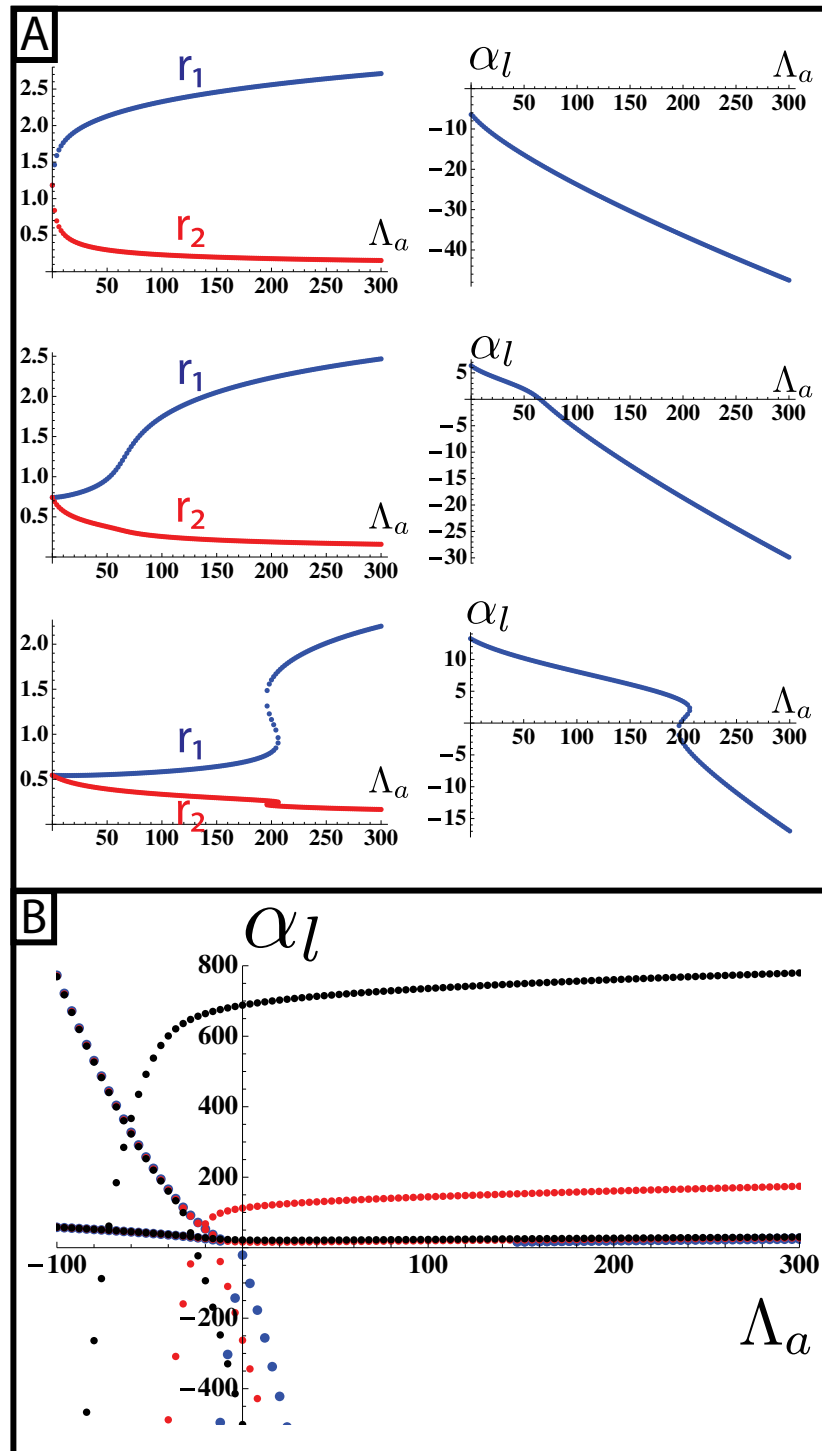


**Fig. S3.** A different hypothesis of shape stabilization: active regulation of the cell–cell tension. (A) (Left) Typical numerical integrations of the basal and apical lengths  $r_1$  and  $r_2$  as a function of apical belt tension  $\Lambda_a$ , for  $\alpha_l = -5$  (Top),  $\alpha_l = 10$  (Middle), and  $\alpha_l = 20$  (Bottom). (Right) Corresponding cell–cell lateral tension, which now changes with  $\Lambda_a$ , because it is actively regulated depending on  $r_1$  and  $r_2$ . We observe the same qualitative effect of cell–cell adhesion as in the main text. Moreover,  $\alpha_l$  undergoes the same type of continuous vs. discontinuous transitions as the geometrical parameters  $r_1$  and  $r_2$ . (B) Evolution of the phase diagram of the 3D architecture of curved epithelia for an active regulation of tensions and for various values of  $\gamma_b = 0$  (blue),  $\gamma_b = -5$  (red), and  $\gamma_b = -15$  (black). Again, the qualitative results of the main text are unchanged.

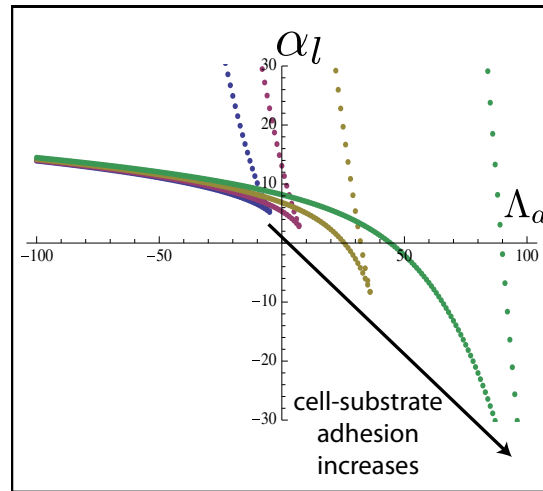


**Fig. S4.** Phase diagram as a function of  $\Lambda_a$  and  $\alpha_l$ , for varying values of  $\gamma_b$ : 0 (blue), -5 (purple), -15 (brown), and -45 (green).

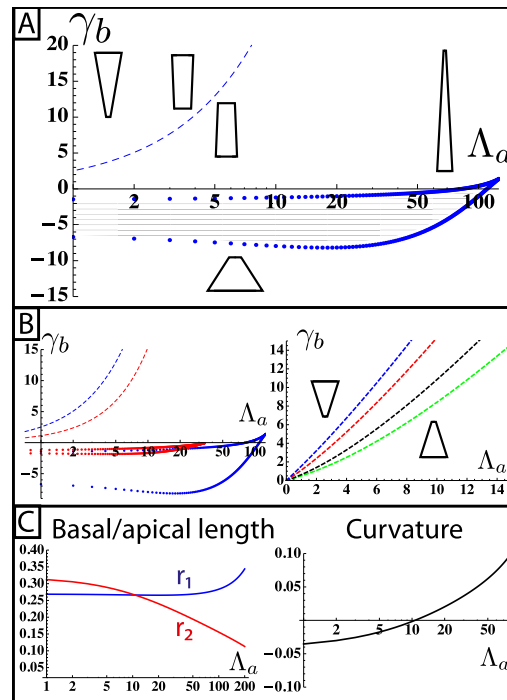


**Fig. S5.** (A) Phase diagram of the 3D architecture of epithelial tissue, as a function of apical belt tension force  $\Lambda_a$  and the basal tension  $\gamma_b$ . We plot both the spinodal lines (blue dots) delimiting bistable equilibria (hatched region) and the separation between negative and positive curvatures (dashed lines). Plot for  $\alpha_l = 6$  is shown. (B) Same phase diagram of the 3D architecture comparing two values of cell-cell adhesion,  $\alpha_l = 6$  (blue) and  $\alpha_l = 4$  (red). Shown is a zoom-in on the frontier separating positive and negative curvature, for various values of cell-cell adhesion:  $\alpha_l = -4$  (green),  $\alpha_l = 0$  (black),  $\alpha_l = 4$  (red), and  $\alpha_l = 6$  (blue). (C) Example of a numerical integration of the basal and apical length (Left) and curvature changing sign (Right) for increasing  $\Lambda_a$ . We chose  $\alpha_l = 6$  and  $\gamma_b = 20$ .

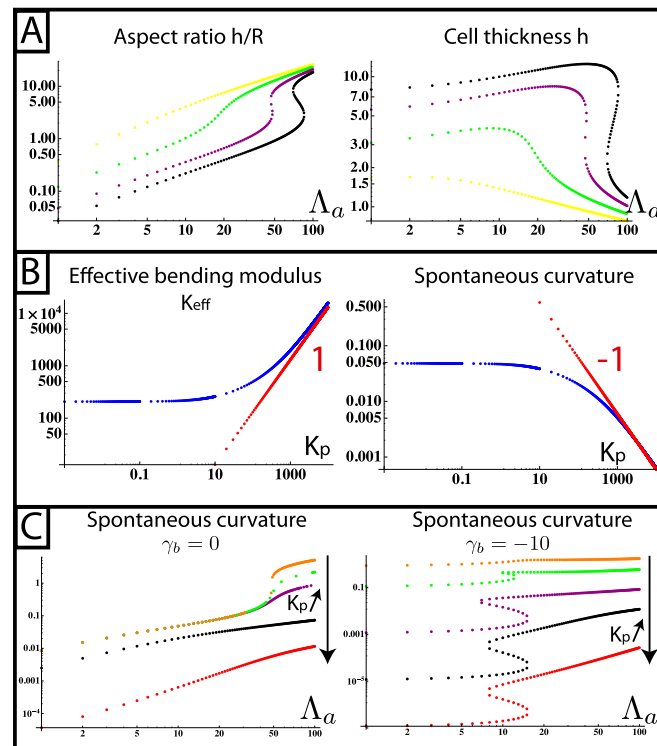


**Fig. S6.** (A) Limit of infinitely soft substrate: aspect ratio of the curved epithelia (height divided by the radius of curvature) and cell thickness, as a function of apical belt tension  $\Lambda_a$ , for various values of  $\alpha_l = 1$  (yellow),  $\alpha_l = 3$  (green),  $\alpha_l = 4.5$  (purple), and  $\alpha_l = 5.5$  (black). (B) For finite elasticities of the substrate, effective bending modulus and spontaneous curvature as a function of the substrate bending modulus  $K_p$ . We use the same parameter set as before:  $\gamma_b = 0$ ,  $\alpha_l = 4.5$ , and  $\Lambda_a = 10$ . (C) Spontaneous curvature of an apically constricted tissue with various substrate bending moduli  $K_p$  and for  $\alpha_l = 4.5$ . (Left)  $\gamma_b = 0$ . For  $K_p = 0$  (orange), the same transition as before is obtained. When  $K_p$  increases [ $K_p = 0.01$  (green),  $K_p = 0.1$  (violet),  $K_p = 100$  (black), and  $K_p = 10,000$  (red)], the curvature decreases as expected, and the discontinuous transition also disappears. (Right)  $\gamma_b = -10$ . When  $K_p$  increases [ $K_p = 0.1$  (orange),  $K_p = 1$  (green),  $K_p = 100$  (violet),  $K_p = 10^4$  (black), and  $K_p = 10^6$  (red)], the curvature also decreases as expected. For  $K \rightarrow \infty$ , we expect to be in the previous limit of a planar epithelial, with a squamous to columnar morphological transition [observed for  $K_p = 10^6$  (red)]. The discontinuous transition disappears when  $K_p$  decreases.

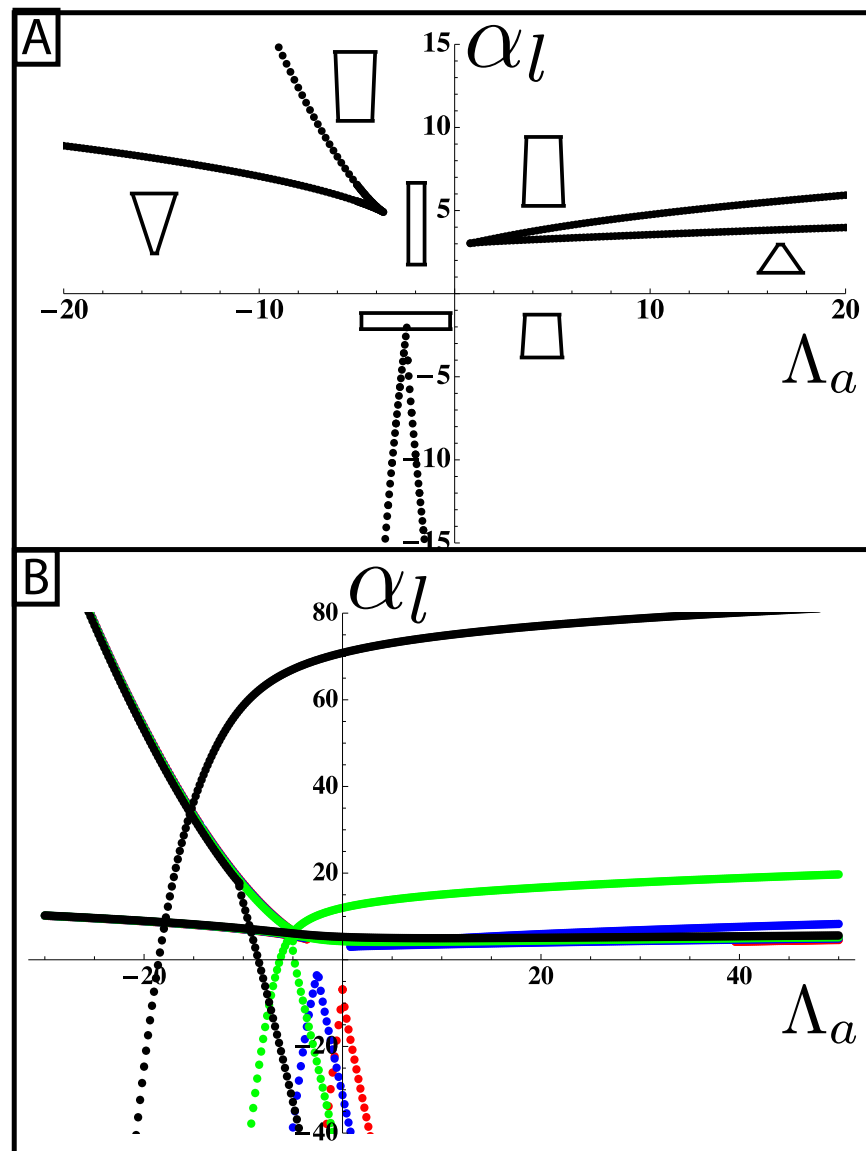


**Fig. S7.** (A) Phase diagram of the 3D architecture of epithelial tissue, as a function of apical belt tension  $\Lambda_a$  and cell-cell adhesion  $\alpha_l$ , for  $\gamma_b = -1$ . (B) Evolution of the phase diagram for various values of  $\gamma_b = 0$  (blue),  $\gamma_b = -1$  (red),  $\gamma_b = -2$  (green), and  $\gamma_b = -4$  (black).

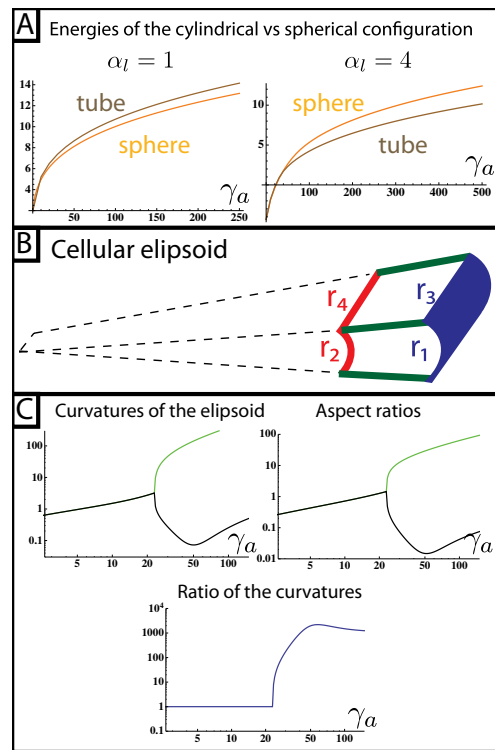


**Fig. S8.** Comparison of the mechanical stability for cellular tubes and spheres. (A) Energies of a sphere and tubes as a function of the apical cortex tension  $\gamma_a$  for  $\alpha_l = 1$  (Left) and  $\alpha_l = 4$  (Right). (B) Schematics of a infinitesimal piece of a cellular ellipsoid. (C) Curvatures ( $\mathcal{C}_1$  and  $\mathcal{C}_2$ ), aspect ratios ( $h\mathcal{C}_1$  and  $h\mathcal{C}_2$ ), and ratios of curvatures of an ellipsoid as a function of apical tension  $\gamma_a$ .

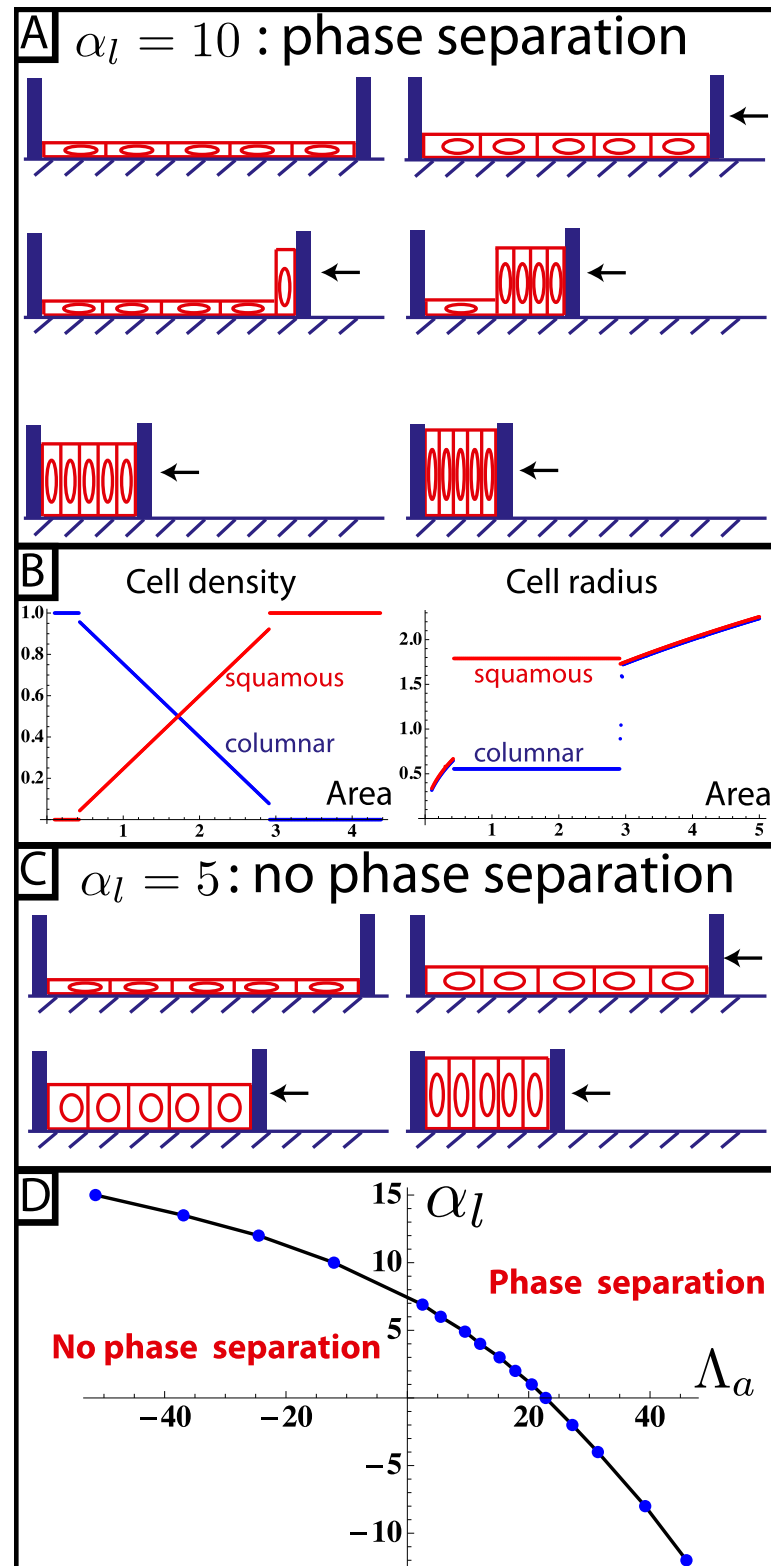


**Fig. S9.** Cell confinement and phase separation. When squamous cells are confined, two scenarios are possible. (A and B) For high values of cell-cell adhesions, a phase separation occurs (A), with squamous and columnar cells maintaining their radii and converting to match the total available area (B). (C) For low values of cell-cell adhesions, the transition is continuous. (D) Diagram of phase separation.